PCCP

PAPER

View Article Online
View Journal | View Issue

Cite this: *Phys. Chem. Chem. Phys.*, 2019, **21**, 8073

What accounts for the color purity of tetradentate Pt complexes? A computational analysis†

Wanlin Cai,[a] Huize Zhang,[a] Xi Yan,[a] Anchong Zhao,[a] Rongxing He,[a] Ming Li,[a] Qingxi Meng[b] and Wei Shen*[a]

In order to improve the texture of human visual perception and broaden the range of certain optical applications, many phosphorescent complexes exhibiting narrow emission spectra have been prepared through reasonable molecular design. For example, by adding a particular group such as *tert*-butyl (*t*bu) to a suitable position of **PtON1** and **PtON7**, the peak width of a relevant vibronic band caused by the specific vibrational normal modes could be dramatically restrained in the emission spectra at room temperature. For the purpose of finding an effective approach to replace the trial-and-error manner, the microscopic mechanism of such high color purity was elucidated by computational investigation. In this study, we aim to identify the reason that causes sharp emission associated with the relevant vibrational normal modes. Here, these modes can be labeled to the emission peak by the vibrationally resolved emission spectra. Based on the displacement vectors of relevant normal modes and the vibrationally resolved spectra, the most possible reason for the higher color purity is that *t*bu in a specific location can restrain the structural deformation between the first triplet excited state (T_1) and the ground state (S_0). That is to say, the relevant Huang–Rhys factor (S_k) of specific vibrational modes would be decreased. For these compounds, the total bandwidth and the height of the intermediate and high-frequency regions which are in direct proportion to S_k would be decreased to obtain the higher color purity by *t*bu in a particular position. What is more, the best position for *t*bu in order to suppress the structural deformation was also considered. In the meantime, radiative (k_r) and nonradiative (k_{nr}) decay rates of T_1 were investigated to seek the effective phosphorescent complexes.

Received 14th February 2019,
Accepted 12th March 2019

DOI: 10.1039/c9cp00819e

rsc.li/pccp

1. Introduction

Phosphorescent organic light-emitting diodes (PhOLEDs) have received significant attention, and tremendous progress has been made with the efforts of many scientists.[1] The spin-forbidden transition between the singlet and triplet states is broken by the heavy element effect of Ir and Pt to utilize all excitons.[2] Notably, a strategy to combine the high efficiency of organometallic materials which are dopants with the long-term stability of thermally activated delayed fluorescence (TADF) compounds was proposed to achieve higher performance in recent research.[3–5] However, most attention has been focused on highly efficient and stable deep blue phosphorescence to further development and application in industry.[6] There still exists a problem about high color purity, which should be further optimized. The full-width at half-maximum (FWHM) values of many metallic compounds with a broad peak are typically between 40 and 70 nm; these complexes would be unsatisfactory in some optical applications.[7] What's more, the broad peak could hinder the further growth of organic electroluminescent devices by compromising the color purities in displays.

Recently, J. Li and co-workers have synthesized a series of tetradentate Pt complexes to solve the problem of high color purity to some extent by suppressing vibronic sidebands of emission spectra.[8–10] Notably, these molecules have great phosphorescence quantum efficiency and outstanding stability that could be used in industrial application. The excellent operational lifetimes are partly caused by the commendable tetradentate cyclometalated structure, without fluorine electron-withdrawing groups that may lead to electrochemical degradation.[11,12] In Li's study, the photoluminescence spectra of **PtON1-*t*bu** and **PtON7-*t*bu** had smaller FWHM values than those of **PtON1** and **PtON7** at ambient temperature. According to Li's opinion, the spectral narrowing was attributed to the increasing energy of the ^{1}MLCT/^{3}MLCT and ^{3}LC states of the carbazole pyridine (CP) moiety, resulting in a larger energy separation to minimize the influence of the CP. Here, to effectively estimate the relevant mechanism of this

[a] *Key Laboratory of Luminescence and Real-Time Analytical Chemistry (Southwest University), Ministry of Education, School of Chemistry and Chemical Engineering, Southwest University, Chongqing 400715, China. E-mail: shenw@swu.edu.cn*
[b] *College of Chemistry and Material Science, Shandong Agricultural University, Taian, Shandong, 271018, China*

† Electronic supplementary information (ESI) available. See DOI: 10.1039/c9cp00819e

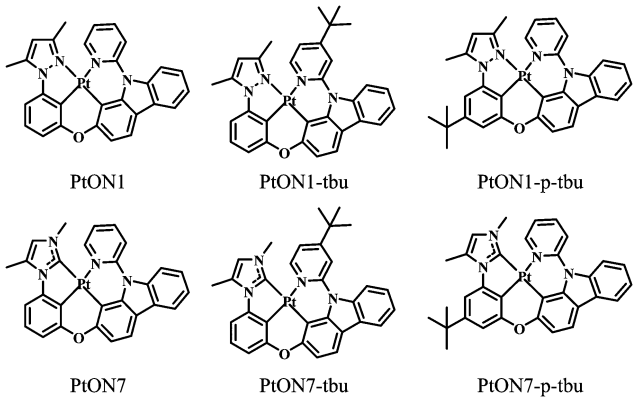

Scheme 1 Chemical structures of studied complexes.

curious phenomenon and deeply understand the photochemistry, quantum mechanical calculation was considered.

How does *t*bu account for this marked difference induced by alteration on the CP? To understand the role of *t*bu more profoundly, **PtON1-*p*-*t*bu** and **PtON7-*p*-*t*bu** were designed to consider the most suitable position for increasing the color purity effectively. All the molecular structures are illustrated in Scheme 1. In this study, it was found that only introducing *t*bu to the 4-position of pyridine could improve the purity of color of these organometallic compounds. Here, the transition dipole moments $\mu_{S_0\rightarrow S_l}$ were plotted to understand whether *t*bu causes the variance of different ligands to obtain high color purity.[13] Furthermore, in order to elucidate the nature of this experimental phenomenon, the mathematical expressions of emission spectra were considered in order to understand the role of the Huang–Rhys factors during the modulation process of color purity. Meanwhile, the relationship between the Huang–Rhys factors of the corresponding vibrational normal modes and the shape of the emission peak was investigated.

2. Computational details

In this article, the geometry optimizations and vibrational frequency calculations of S_0 and T_1 were calculated by using the restricted density functional theory (DFT) and unrestricted DFT with the PBE0 hybrid functional.[14] The 6-31G** basis and the LANL2DZ basis were respectively adopted for the light atoms and transition metal atom Pt. The relevant calculations were carried out using the program Gaussian 09 with the polarizable continuum model (PCM) in CH_2Cl_2.[15] The MECP was obtained *via* the program sobMECP, which was modified by Tian Lu.[16,17] The program multiwfn[18] and the software VMD[19] were employed to plot the vectors of transition dipole moments together.

As the conventional sum-over-state (SOS) method is slowly convergent when considering bulky transition metal complexes, response function theory containing the electric dipole and spin–orbit operators was employed to enhance the effectiveness of the calculations.[20,21] The transition dipole moment and the spin–orbit coupling matrix element between T_1 and S_0 were respectively calculated by using the quadratic response and the linear response with single residue. The spin–orbit coupling matrix elements and the singlet–triplet splitting energies between S_l and T_1 were evaluated *via* the linear response with double residue. These calculations mentioned above were obtained with the assistance of the program Dalton 2016.[22] The non-equilibrium contributions of the solvent to the response calculation were used for the PCM.

On the basis of the relevant information obtained above, the phosphorescence spectra, the radiative rate and the intersystem crossing rate were computed using the program MOMAP.[23]

3. Results and discussion

3.1 Electronic transition properties

Natural transition orbital (NTO) analysis, illustrated in Fig. S1 (ESI†), was computed to depict the motion of electrons from occupied NTOs (holes) to unoccupied NTOs (electrons). Here, **PtON1-*t*bu** and **PtON7-*t*bu** could have smaller k_r than their respective homologs, since they have a lower proportion of ^{3}MLCT as shown in Fig. S1 (ESI†).[24] However, the roles that different ligands play cannot be clear from NTO analysis.

Based on the time-dependent perturbation method, the transition dipole moment of $\mu_{T_1\rightarrow S_0}$ can be expressed as

$$\mu_{T_1\rightarrow S_0} = \sum_{l\in \text{singlets}} \frac{\langle S_0|\hat{\mu}|S_l\rangle\langle S_l|\hat{H}^{SO}|T_1\rangle}{E_{T_1} - E_{S_l}} + \sum_{n\in \text{triplets}}\sum_{j=-1,0,1} \frac{\langle S_0|\hat{H}^{SO}|T_{n,j}\rangle\langle T_{n,j}|\hat{\mu}|T_1\rangle}{E_{S_0} - E_{T_n}}, \quad (1)$$

where the second term could be ignored due to the relatively large energy gaps between T_n and S_0.[25] Therefore, it is reasonable to plot the transition dipole moments $\mu_{S_0\rightarrow S_l}$ of the first term in order to understand the role of various kinds of ligands during the process from excitation to deexcitation.

In view of the fact that many electronic states are involved during transition processes, it is necessary to find the crucial electronic states connected with the transition dipole moments ($\mu_{S_0\rightarrow S_l}$), the spin–orbit coupling matrix elements ($\langle S_l|\hat{H}^{SO}|T_1\rangle$) and the singlet–triplet splitting energies ($\Delta E_{S_l-T_1}$). Here, the crucial electronic states denote that the singlet excited states have a relatively large contribution to $\mu_{T_1\rightarrow S_0}$ according to eqn (1). All of the above parameters for $\mu_{T_1\rightarrow S_0}$ are listed in Table 1. For all studied compounds, the vectors of transition dipole moments for the whole compound and for different ligands, which are phenyl pyrazole (PP) and carbazole pyridine (CP) in **PtON1** and its derivatives in combination with phenyl imidazole (PI) and carbazole pyridine in **PtON7** and its derivatives, were plotted in Fig. S2–S7 (ESI†). What is more, the vectors of plotted dipole moments of the main electronic states in **PtON1-*t*bu** and **PtON7-*t*bu** are shown in Fig. 1.

As shown, the electronic states S_2, S_7 and S_9 with their relatively large contribution are significant in the transition processes for **PtON1-*t*bu**. In Fig. 1, the direction and value of $\mu_{S_0\rightarrow S_2}$ and $\mu_{S_0\rightarrow S_7}$, the essential parameters for excitation, attributed to PP and CP have a similar contribution to the whole complex.[13] For **PtON7-*t*bu**, the contribution of PI and CP for the critical excited

Table 1 Calculated transition dipole moments $\mu_{S_0\rightarrow S_i}$ (Debye), singlet–triplet splitting energies $\Delta E_{S_i-T_1}$ (eV), the SOC matrix elements $\langle S_i|\hat{H}^{SO}|T_1\rangle$ (cm^{-1}) and the contribution of each excited state to $\mu_{T_1\rightarrow S_0}$ (Debye)

	$\mu_{S_0\rightarrow S_i}$	$\Delta E_{S_i-T_1}$	$\langle T_1\|\hat{H}^{SO}\|S_i\rangle$	Contribution	$\mu_{S_0\rightarrow S_i}$	$\Delta E_{S_i-T_1}$	$\langle T_1\|\hat{H}^{SO}\|S_i\rangle$	Contribution	$\mu_{S_0\rightarrow S_i}$	$\Delta E_{S_i-T_1}$	$\langle T_1\|\hat{H}^{SO}\|S_i\rangle$	Contribution
	PtON1				**PtON1-*t*bu**				**PtON1-*p*-*t*bu**			
S_1	1.88	0.17	115.23	0.1551	2.17	0.60	30.89	0.0138	2.17	0.17	133.42	0.2096
S_2	4.56	0.54	453.29	0.4724	4.48	0.98	227.48	0.1291	4.83	0.52	495.92	0.5671
S_3	0.71	0.99	225.43	0.0199	0.67	1.02	74.22	0.0060	0.84	0.96	294.00	0.0318
S_4	1.01	1.02	293.14	0.0361	1.53	1.14	35.26	0.0059	0.94	1.02	84.22	0.0096
S_5	0.90	1.19	1455.91	0.1364	2.57	1.27	36.10	0.0091	0.66	1.19	1511.57	0.1044
S_6	1.64	1.25	303.84	0.0494	0.91	1.39	191.49	0.0155	1.43	1.25	264.16	0.0375
S_7	0.76	1.32	271.93	0.0194	6.86	1.41	119.49	0.0719	1.58	1.33	298.38	0.0441
S_8	8.59	1.39	62.38	0.0479	2.61	1.59	63.81	0.0130	8.48	1.40	72.50	0.0546
S_9	2.56	1.47	85.60	0.0184	1.92	1.65	609.85	0.0876	2.27	1.47	95.36	0.0183
S_{10}	0.14	1.55	246.13	0.0028	0.09	1.73	153.65	0.0010	0.30	1.52	230.59	0.0057
	PtON7				**PtON7-*t*bu**				**PtON7-*p*-*t*bu**			
S_1	2.27	0.19	125.44	0.1828	2.63	0.55	24.23	0.0144	2.74	0.19	150.44	0.2670
S_2	3.96	0.60	420.55	0.3410	3.26	0.90	121.83	0.0546	4.36	0.59	483.15	0.4441
S_3	1.16	0.88	138.67	0.0227	1.57	1.02	168.68	0.0323	0.93	0.88	296.60	0.0387
S_4	0.85	0.96	386.02	0.0424	1.22	1.12	28.98	0.0039	0.83	0.95	221.97	0.0241
S_5	0.10	1.19	990.41	0.0104	0.36	1.25	11.92	0.0004	0.07	1.19	1252.46	0.0097
S_6	1.73	1.24	1038.35	0.1797	1.12	1.29	156.33	0.0167	0.47	1.24	910.64	0.0427
S_7	2.03	1.37	507.20	0.0928	6.09	1.42	155.69	0.0825	4.36	1.36	530.38	0.2106
S_8	9.06	1.39	181.34	0.1464	5.74	1.60	638.07	0.2845	8.53	1.41	153.87	0.1152
S_9	2.17	1.47	189.12	0.0346	2.62	1.61	194.01	0.0390	1.84	1.41	178.30	0.0289
S_{10}	0.25	1.59	242.21	0.0048	0.19	1.69	189.31	0.0027	0.16	1.56	276.86	0.0036

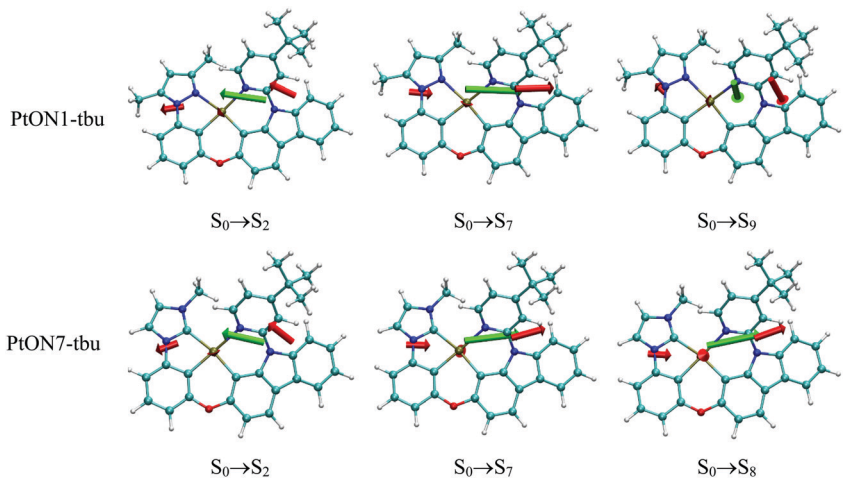

Fig. 1 The contributions from different ligands to the transition dipole moment $\mu_{S_0\rightarrow S_i}$ were plotted for **PtON1-*t*bu** and **PtON7-*t*bu**. The vectors of PI, PP, CP and Pt atom are marked in red. At the same time, the whole compound vectors are marked in green. The length of the arrow indicates the magnitude of the dipole moment.

states S_2, S_7 and S_8, is similar. The same conclusions can be drawn from the analysis of other molecules in Fig. S2–S7 (ESI†).

Clearly, these ligands, including CP, PP and PI, have a similar influence on the transition processes. Therefore, we could not simply consider Li's opinion that the spectral narrowing is caused by the introduction of CP resulting in larger energy separation.

3.2 Emission spectra

Thanks to recent developments of computational chemistry, it is convenient to simulate the phosphorescence spectra, which are helpful in understanding the luminescent properties of transition-metal complexes.[23,26] In particular, the vibrationally resolved emission spectra calculated can be used to verify the contribution of the vibrational normal modes to the relevant emission bands. All the spectra mentioned above were evaluated in Fig. 2 and 3 to understand the origin underlying the markedly different color purity induced by alterations in ligands. In view of the fact that we focus on the color purity rather than on the absolute intensities of the phosphorescent emission, the spectra in Fig. 2 and 3 were normalized by taking the maximum peaks with equal height for a better comparison of the band shape.[27] Compared with PtON1 and PtON7, the bandwidths of **PtON1-*t*bu** and **PtON7-*t*bu** are obviously weakened after adding *t*bu to the 4-position of the pyridine ring. Meanwhile, there is no apparent change in the intensity of relevant vibronic bands after adding *t*bu to the 4-position of the benzene ring.

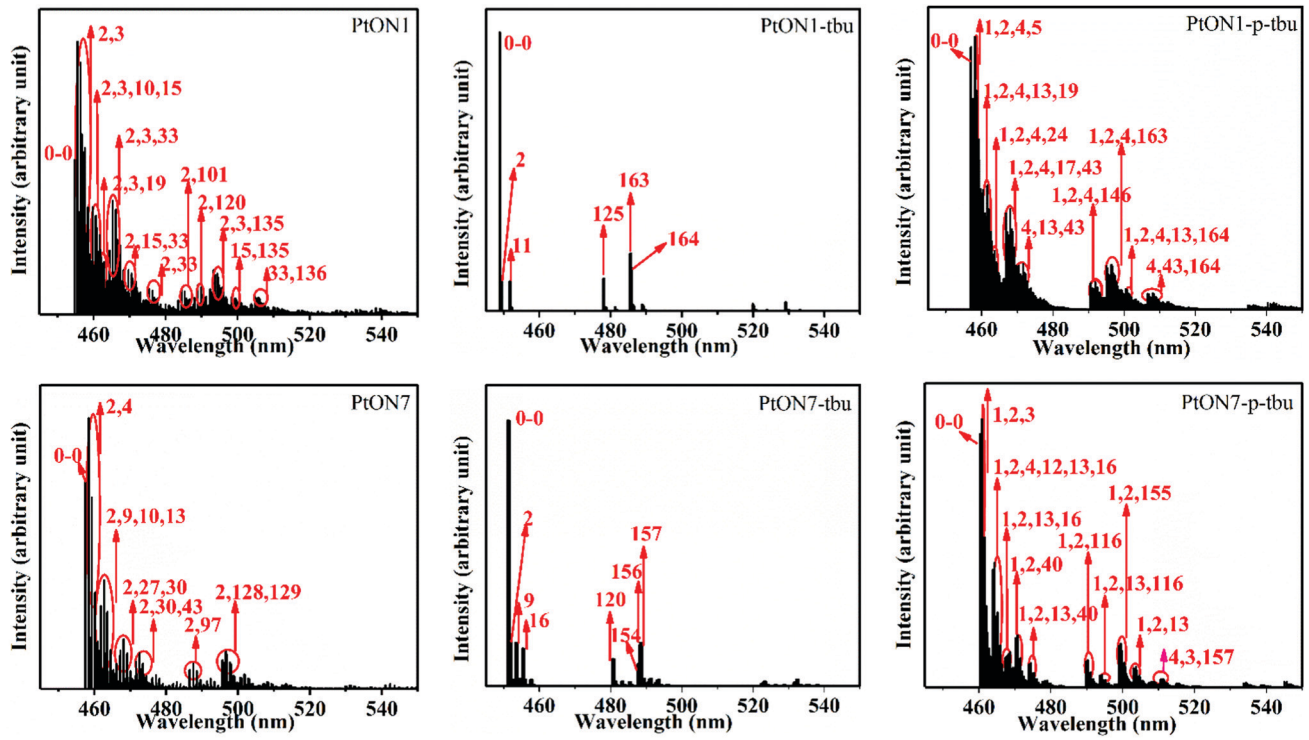

Fig. 2 The calculated vibrationally resolved emission spectra at 0 K.

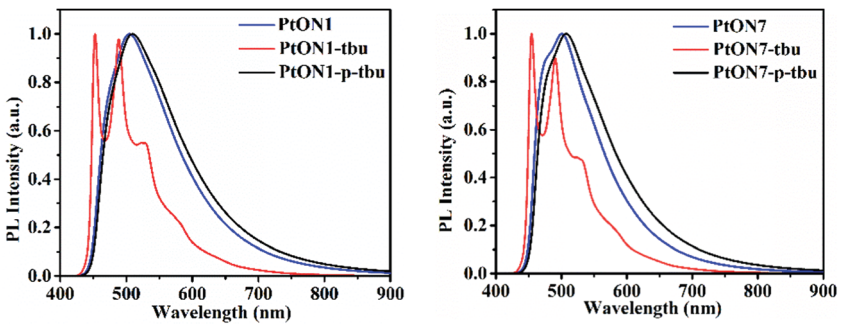

Fig. 3 The calculated phosphorescent emission spectra at room temperature.

For a strong coupling case where the short-time approximation is conducted, the quantum mechanical definition of the emission coefficient that is the mathematical expression of the emission spectra[28] can be expressed as

$$\alpha_{T_1\to S_0} = \frac{2\pi\omega}{3\hbar ca}\left|\mu_{T_1\to S_0}\right|^2 \sqrt{\frac{4\pi}{D^2 + 2\sum_k (2\bar{n}_k + 1)S_k\omega_k^2}} \exp\left[-\frac{\left(\omega - \bar{\omega}_{T_1\to S_0} + \sum_k S_k\omega_k\right)^2}{D^2 + 2\sum_k (2\bar{n}_k + 1)S_k\omega_k^2}\right], \quad (2)$$

where the factor a is introduced to take into account the solvent effect and $\bar{n}_k = (e^{\hbar\omega_k/k_BT} - 1)^{-1}$ denotes the phonon distribution. The maximum emission is $\omega_{T_1\to S_0} - \sum_k S_k\omega_k$. Meanwhile, the emission spectra show that the bandwidth $\left(2\sqrt{2\ln\left[D^2 + 2\sum_k (2\bar{n}_k + 1)S_k\omega_k^2\right]}\right)$ increases with T, where D represents the consideration of the inhomogeneous broadening.

As is shown, the bandwidth is proportional to the Huang–Rhys factors. The band would be broadened for organometallic compounds with bigger total Huang–Rhys factors, especially when temperatures rise.[29] Considering all vibrational normal modes, a diminution of the Huang–Rhys factors would cause a

narrowing of the emission peak. Therefore, the smaller total Huang–Rhys factors contribute to the lower bandwidth for **PtON1-*t*bu** and **PtON7-*t*bu**. Here, it should be noted that the emission of **PtON1**, **PtON1-*p*-*t*bu**, **PtON7** and **PtON7-*p*-*t*bu** should have at least two peaks according to Fig. 2. However, there is only one obvious broad peak of these compounds in Fig. 3. The primary factor behind the phenomena could be attributed to the inhomogeneous broadening effect produced by combination with low-frequency modes and high-frequency modes,[27,30] for the temperature effect on systems with larger Huang–Rhys factors is so great.

Closely associated with the Huang–Rhys factors, the well-known Franck–Condon factors (Scheme 2a), the square of the vibrational overlap integral between T_1 and S_0, determine the emission strength.[31,32] Here, another representation of the emission coefficient can be represented as

$$\alpha_{T_1\rightarrow S_0} = \frac{4\pi^2\omega}{3\hbar ca}\left|\mu_{T_1\rightarrow S_0}\right|^2\sum_{v_k}\left(\prod_k \frac{S_k^{v_k}}{v_k!}e^{-S_k}\right)D\left(\omega_{S_{0,v_k},T_{1,0}} - \omega\right). \quad (3)$$

For simplicity, the Franck–Condon factor $I_{S_{0,k},T_{1,0}}$ is evaluated at 0 K. In this case, we have

$$I_{S_{0,v_k},T_{1,0}} = \left|\left\langle \chi_{S_{0,k}} \middle| \chi_{T_{1,0}} \right\rangle\right|^2 = \frac{S_k^{v_k}}{v_k!}e^{-S_k}, \quad (4)$$

where v_k represents the vibrational quantum number of the kth vibrational normal mode. More relations about the peak intensity can be obtained in general as follows:

$$\ln I_{S_{0,k},T_{1,0}} = v_k \ln S_k - S_k - v_k \ln v_k + v_k; \quad (5)$$

$$\frac{\partial}{\partial S_k}\ln I_{S_{0,k},T_{1,0}} = \frac{v_k}{S_k} - 1. \quad (6)$$

Some useful results can be acquired by setting $\frac{\partial}{\partial S_k}\ln\frac{S_k^{v_k}}{v_k!}e^{-S_k} = 0$.[32] That is to say, the maximum of $I_{S_{0,k},T_{1,0}}$ can be obtained when $v_k = \lfloor S_k \rfloor$. In this case, the fractions of S_k rounded down to 0 are denoted by $\lfloor S_k \rfloor$. Furthermore, the Franck–Condon factor of $v_k = \lfloor S_k \rfloor$ is higher than $v_k = 0$ when $S_k > 1$. When $S_k < 1$, $I_{S_{0,k},T_{1,0}}$ is the maximum by taking $v_k = 0$ when $S_k < 1$. For the relevant vibrational modes associated with the pyridine ring, the Huang–Rhys factors of the intermediate and lower-energy region are lower than 1. As shown in Scheme 2a, for a Huang–Rhys factor lower than 1 when $v_k > 0$, the Franck–Condon factor is proportional to the Huang–Rhys factor. Here, the emission intensity of **PtON1-*t*bu** and **PtON7-*t*bu** in these areas would be relatively weaker than the 0–0 peak by the diminution of the Huang–Rhys factor for the lower structural deformation. To be sure, the Franck–Condon factors depend on the Huang–Rhys factors. Furthermore, based on the lower height of the intermediate and lower-energy regions, the whole spectra would be pure blue. That is to say, the weaker emission band shape, including bandwidth and peak intensity, is directly decided by the lower Huang–Rhys factors.

What is the reason for the difference after the alteration on the pyridine and benzene by *t*bu? Based on the fact that only adding *t*bu to the 4-position of the pyridine can increase the purity, the vibrational normal modes' displacement vectors of **PtON1** and **PtON1** that are mainly involved in the emission spectra are shown in Fig. S9 and S10 (ESI†) to reveal the secret. As shown, the high-frequency modes 101, 120, 135 and 136 for **PtON1** combined with 97, 128 and 129 for **PtON7** contributing to the emission spectra are more closely connected with the pyridine rather than the benzene ring. What's more, the 33 mode for **PtON1** and the 30 and 43 modes for **PtON7**, only associated with pyridine, contribute to the intermediate emission region between the two main spectral bands in Fig. 3.

Once *t*bu is added to the pyridine ring, structural deformation of relevant vibrational modes could be effectively restrained.[33,34] In Scheme 2b, the Huang–Rhys factor can be expressed as $S_k = \frac{\omega_k}{2\hbar}\Delta Q_k^2$, where ΔQ_k is the vibrational displacement in nuclear coordinates between the initial and final state. As shown in Table 2, the smaller root mean square deviation (RMSD) associated with ΔQ_k could indicate that the structural deformation of **PtON1-*t*bu** and **PtON7-*t*bu** between T_1 and S_0 will be more restrained than their parent compounds. That is to

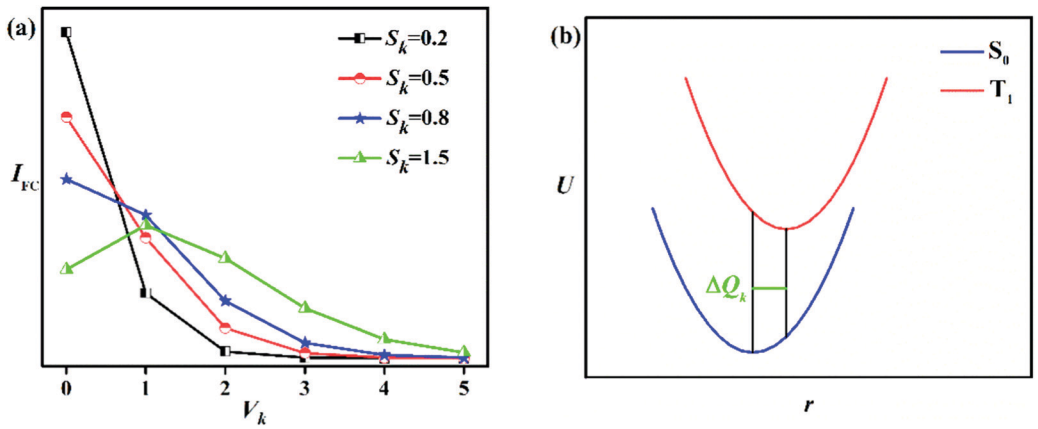

Scheme 2 (a) The Franck–Condon factors for the vibrational normal modes with different Huang–Rhys factors. Here, v_k represents the vibrational quantum numbers. (b) The relationship between ΔQ_k and the Huang–Rhys factor S. It should be noted that the ΔQ_k for each vibrational mode is different.

Table 2 The root mean square displacement of S_0 and T_1 for all complexes

Complexes	PtON1	PtON1-*t*bu	PtON1-*p*-*t*bu	PtON7	PtON7-*t*bu	PtON7-*p*-*t*bu
RMSD	0.100	0.048	0.144	0.115	0.055	0.134

say, the Huang–Rhys factor of these vibrational modes would be decreased. What is more, the total bandwidth and the height of the intermediate and high-frequency regions for these organometallic complexes, which are contributed by the involved vibrational modes associated with the pyridine ring, would be weakened (Tables 3 and 4).

It should be noted that the number of vibrational normal modes related to total Huang–Rhys factors are directly proportional to the atomic number. The position for *t*bu to replace H atom can't be random, for example, **PtON1-*p*-*t*bu** and **PtON7-*p*-*t*bu**. Otherwise, color purity would be decreased by the larger total Huang–Rhys factors. Fortunately, the vibrationally resolved emission spectra can help us to estimate the appropriate site.

3.3 Radiative and nonradiative decay rates

To further explore the effectiveness of these compounds, the photoluminescence quantum yield (PLQY),[35] an indispensable part of the emissive properties, was also obtained by

$$\Phi(T) = \frac{k_r}{k_r + k_{ISC} + k_{nr}(T)}, \quad (7)$$

where k_r denotes the radiative decay rate, and k_{ISC} and $k_{nr}(T)$ represent the intersystem crossing rate and the temperature-dependent nonradiative rate, respectively.

Table 4 Experimental and theoretical photoluminescence properties

	k_r/s^{-1} (cal)	k_{ISC} (cal)	k_r/s^{-1} (exp)	k_{nr}/s^{-1} (exp)	Φ (exp)
PtON1	3.72×10^5	6.83×10^4	$(2.15 \times 10^5)^a$	$(8.79 \times 10^4)^a$	0.71
PtON1-*t*bu	0.73×10^5	1.35×10^4	$(1.07 \times 10^5)^a$	$(0.56 \times 10^4)^a$	0.95
PtON1-*p*-*t*bu	3.78×10^5	10.30×10^4			
PtON7	3.12×10^5	0.68×10^4	$(1.86 \times 10^5)^a$	$(5.24 \times 10^4)^a$	0.78
PtON7-*t*bu	0.96×10^5	0.25×10^4	$(1.26 \times 10^5)^b$	$(2.22 \times 10^4)^b$	0.83
PtON7-*p*-*t*bu	2.84×10^5	1.65×10^4			

[a] Ref. 42. [b] Ref. 7.

What is more, k_r was obtained by the Einstein A coefficient of spontaneous emission,

$$k_r(T_1 \rightarrow S_0) = \frac{8\pi^2\eta^3(E_{T_1} - E_{S_0})^3}{3\varepsilon_0\hbar}\left|\mu_{T_1 \rightarrow S_0}\right|^2. \quad (8)$$

According to Peng's works,[36] the intersystem crossing rate based on Fermi's golden rule can be formulated as

$$\ln[k_{ISC}(T_1 \rightarrow S_0)] = \frac{\left(E_{T_1} - E_{S_0} - \sum_k \lambda_k\right)}{4\sum_k \lambda_k \bar{E}_k} + \ln\left(\frac{1}{\hbar}\left|\langle S_0|\hat{H}^{SO}|T_1\rangle\right|^2 \sqrt{\frac{\pi}{\sum_k \lambda_k \bar{E}_k}}\right), \quad (9)$$

where λ_k, defined by $\lambda_k = S_k\hbar\omega_k$, is the reorganization energy of the kth vibrational normal mode. In addition, to fully understand the nonradiative decay process, the thermal deactivation

Table 3 The calculated frequency, reorganization energy and the Huang–Rhys factor of the normal modes mainly involved in the vibrationally resolved spectra

Mode	ω	λ	S	Mode	ω	λ	S	Mode	ω	λ	S
PtON1				**PtON1-*t*bu**				**PtON1-*p*-*t*bu**			
2	40.08	77.27	1.93	2	27.51	2.97	0.11	1	21.59	17.17	0.80
3	58.1	40.35	0.69	11	139.92	0.72	0.11	2	28.36	22.4	0.79
9	142.06	20.93	0.15	125	1359.91	3.54	0.14	4	54.75	60.79	1.11
10	162.13	36.65	0.23	163	1684.27	0.68	0.27	5	62.34	8.97	0.14
11	171.97	16.57	0.10	164	1694.81	4.31	0.20	13	163.33	82.35	0.50
15	200.07	82.39	0.41					17	198	45.42	0.23
19	250.41	82.71	0.33					19	215.25	55.95	0.26
33	458.11	210.41	0.46					24	260.53	59.25	0.23
101	1305.26	146.31	0.11					43	460.05	183.92	0.40
120	1497.13	199.35	0.13					146	1498.47	188.5	0.13
135	1681.53	351.21	0.21					163	1681.4	356.49	0.21
136	1693.22	314.39	0.19					164	1693.06	344.21	0.20
PtON7				**PtON7-*t*bu**				**PtON7-*p*-*t*bu**			
2	42.49	62.06	1.46	1	22.7	2.89	0.13	1	22.76	24.67	1.08
4	77.37	19.35	0.25	2	30.45	5.23	0.17	2	36.16	20.36	0.56
9	153.77	17.95	0.12	9	114	19.26	0.17	3	42.06	9.34	0.22
10	163.69	32.84	0.20	16	202.12	29.42	0.15	4	57.1	15.02	0.26
13	202.82	85.55	0.42	120	1357.32	165.48	0.12	6	75.64	15.31	0.20
27	403.39	55.61	0.14	154	1665.16	177.97	0.11	12	154.77	19.65	0.13
30	456.13	92.77	0.20	156	1683.5	330.43	0.20	13	164.53	81.44	0.49
43	653.07	95.72	0.15	157	1694.01	351.46	0.21	16	202.08	59.58	0.29
97	1303.38	147.22	0.11					40	459.02	98.52	0.21
128	1680.65	296.15	0.18					116	1304.45	160.47	0.12
129	1692.67	274.17	0.16					155	1680.3	352.46	0.21
								157	1692.48	292.8	0.17

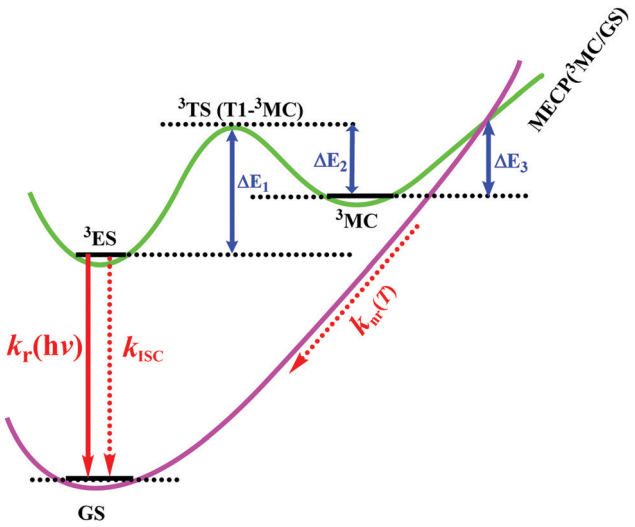

Scheme 3 Schematic of the competing T_1 deactivation processes of Pt(II) complexes.

about $k_{nr}(T)$ *via* ^{3}MC was also discussed. Once the ^{3}MC is formed, there are two main pathways for energy dissipation, either returning back to the ^{3}ES or relaxing to the GS. The latter route is determined by the ^{3}MC/GS minimum energy crossing point (MECP).[35,37] The activation energy ($\Delta E_{lim} = \Delta E_1 - \Delta E_2 + \Delta E_3$) is an important parameter to estimate $k_{nr}(T)$ (Scheme 3).[38,39] The value of ΔE_1, associated with the rate-determining step, and ΔE_{lim} are inversely proportional to $k_{nr}(T)$. The whole kinetic scenario can be depicted as

$$^3\text{MLCT} \underset{k_2}{\overset{k_1}{\rightleftharpoons}} {}^3\text{MC} \xrightarrow{k_3} \text{GS}. \quad (10)$$

Eqn (9) indicates that the k_{ISC} increases with the degree of vibronic coupling deepening, the SOC interaction enhancing and the energy gap narrowing between T_1 and S_0.[24,40] All the calculated results connected to k_{ISC} are listed in Table 5. As shown, **PtON1-*t*bu** and **PtON7-*t*bu** have the lowest k_{ISC} in their respective homologues, in accordance with the higher PLQY. For organic emitting materials, vibronic coupling associated with the Huang–Rhys factors has been found to be the foremost factor for k_{ISC}.[25,41] That is to say, the lower structural deformation of **PtON1-*t*bu** and **PtON7-*t*bu** could be responsible for the smaller k_{ISC}. What is more, the computed results about the energy gap in Table 5 reveal that the $k_{nr}(T)$ of **PtON1-*t*bu** and **PtON7-*t*bu** would be similar to their respective homologues, on account of the approximated ΔE_{lim} and ΔE_1.

Therefore, based on the combination of k_{ISC} and $k_{nr}(T)$, the lower Huang–Rhys factors associated with structural deformation play a significant part for **PtON1-*t*bu** and **PtON7-*t*bu** in obtaining the higher PLQY in these systems.

Table 5 The $\Delta E(T_1-S_0)$ (eV), $\langle S_0|\hat{H}^{SO}|T_1\rangle$ (cm^{-1}) and the total Huang–Rhys factors ($\sum S$) for the intersystem crossing rate. The activation barriers of ΔE_1, ΔE_2, ΔE_3 and ΔE_{lim} (kcal mol^{-1}) for the temperature-dependent nonradiative deactivation channels

	$\Delta E_{T_1-S_0}$	$\langle S_0\|\hat{H}^{SO}\|T_1\rangle$	$\sum_k S_k$	ΔE_1	ΔE_2	ΔE_3	ΔE_{lim}
PtON1	2.864	189.94	4.89	15.87	7.72	4.73	12.88
PtON1-*t*bu	2.904	75.31	2.64	15.27	8.04	5.02	12.25
PtON1-*p*-*t*bu	2.853	192.83	5.70	16.04	7.72	4.63	12.95
PtON7	2.847	126.70	6.40	17.15	8.39	3.88	12.64
PtON7-*t*bu	2.889	45.87	2.63	16.68	8.78	4.12	12.02
PtON7-*p*-*t*bu	2.830	136.34	6.84	17.24	8.43	4.17	12.98

4. Conclusions

In this study, quantum mechanical calculation has been used to successfully rationalize the curious phenomenon about color purity and to estimate the efficiency of these phosphorescent materials.

Based on the plotted transition dipole moment $\mu_{S_0\rightarrow S_i}$, PI, PP and CP of these organometallic complexes have a similar influence on the transition process, for these ligands have similar contributions to $\mu_{T_1\rightarrow S_0}$. In other words, the view that *t*bu results in energy separation to obtain high color purity could be unreasonable. Furthermore, we have successfully unveiled the relation between color purity and structural change through vibrationally resolved emission spectra. For the result that the structural deformation would be restricted by adding a particular group (*t*bu) to the 4-position of the pyridine, the relevant Huang–Rhys factor of specific vibrational modes would be decreased. To put it another way, the total bandwidth and the height of the intermediate and high-frequency regions for these organometallic complexes, which are linked with the pyridine ring, can be diminished. In the meantime, the higher PLQY of **PtON1-*t*bu** and **PtON7-*t*bu** comes from the dramatic decline of k_{ISC} which is associated with the Huang–Rhys factors.

That is to say, the improvement of efficiencies and color purity could be attributed to the decreased Huang–Rhys factors. For future molecular synthesis of high color purity materials, vibrationally resolved emission spectra could be used to estimate and search for an appropriate way to obtain narrow emission bands. Our study could provide an idea for the future design and manufacture of new electroluminescent materials with high color purity.

Conflicts of interest

There are no conflicts to declare.

Acknowledgements

This work was funded by the Chongqing Research Program of Basic Research and Frontier Technology (No. cstc2018jcyjAX0004).

References

1 O. Ostroverkhova, *Chem. Rev.*, 2016, **116**, 13279–13412.
2 F. Neese, *J. Am. Chem. Soc.*, 2006, **128**, 10213–10222.
3 Z. Yang, Z. Mao, Z. Xie, Y. Zhang, S. Liu, J. Zhao, J. Xu, Z. Chi and M. P. Aldred, *Chem. Soc. Rev.*, 2017, **46**, 915–1016.
4 H. Fukagawa, T. Oono, Y. Iwasaki, T. Hatakeyama and T. Shimizu, *Mater. Chem. Front.*, 2018, **2**, 704–709.

5 C. Yao, Y. Z. Yang, L. Li, M. L. Bo, C. Peng and J. S. Wang, *J. Mater. Chem. C*, 2018, **6**, 6146–6152.
6 J. Lee, H.-F. Chen, T. Batagoda, C. Coburn, P. I. Djurovich, M. E. Thompson and S. R. Forrest, *Nat. Mater.*, 2015, **15**, 92.
7 G. Li, T. Fleetham, E. Turner, X. C. Hang and J. Li, *Adv. Opt. Mater.*, 2015, **3**, 390–397.
8 X. C. Hang, T. Fleetham, E. Turner, J. Brooks and J. Li, *Angew. Chem.*, 2013, **125**, 6885–6888.
9 T. Fleetham, G. Li, L. Wen and J. Li, *Adv. Mater.*, 2014, **26**, 7116–7121.
10 T. Fleetham, G. Li and J. Li, *Adv. Mater.*, 2017, **29**, 1601861.
11 W. Song and J. Y. Lee, *Adv. Opt. Mater.*, 2017, **5**, 1600901.
12 S. Scholz, D. Kondakov, B. Lüssem and K. Leo, *Chem. Rev.*, 2015, **115**, 8449.
13 Y. Chen, A. Ren, Z. Yang, T. He, X. Ding, H. Zhang and L. Zou, *Phys. Chem. Chem. Phys.*, 2018, **20**, 9419–9428.
14 C. Adamo and V. Barone, *J. Chem. Phys.*, 1999, **110**, 6158–6170.
15 M. J. Frisch, G. W. Trucks, H. B. Schlegel, G. E. Scuseria, M. A. Robb, J. R. Cheeseman, G. Scalmani, V. Barone, G. A. Petersson, *et al.*, *Gaussian 09, Revision D.01*, Gaussian, Inc., Wallingford, CT, 2013.
16 J. N. Harvey, M. Aschi, H. Schwarz and W. Koch, *Theor. Chem. Acc.*, 1998, **99**, 95–99.
17 T. Lu, website: http://sobereva.com/286.
18 T. Lu and F. Chen, *J. Comput. Chem.*, 2012, **33**, 580–592.
19 W. F. Humphrey, A. Dalke and K. Schulten, *J. Mol. Graphics*, 1996, **14**(33–38), 27–38.
20 J. Olsen and P. Jorgensen, *J. Chem. Phys.*, 1985, **82**, 3235–3264.
21 O. Vahtras, H. Ågren, P. Jorgensen, H. J. R. A. Jensen, T. Helgaker and J. Olsen, *J. Chem. Phys.*, 1992, **97**, 9178–9187.
22 Dalton, a molecular electronic structure program, Release Dalton v2016, 2015, see http://daltonprogram.org.
23 Y. Niu, W. Li, Q. Peng, H. Geng, Y. Yi, L. Wang, G. Nan, D. Wang and Z. Shuai, *Mol. Phys.*, 2018, 1–13.
24 A. M. Prokhorov, T. Hofbeck, R. Czerwieniec, A. F. Suleymanova, D. N. Kozhevnikov and H. Yersin, *J. Am. Chem. Soc.*, 2014, **136**, 9637–9642.
25 Q. Peng, Q. Shi, Y. Niu, Y. Yi, S. Sun, W. Li and Z. Shuai, *J. Mater. Chem. C*, 2016, **4**, 6829–6838.
26 X. Zheng, Q. Peng, L. Zhu, Y. Xie, X. Huang and Z. Shuai, *Nanoscale*, 2016, **8**, 15173–15180.
27 F. D. Angelis, F. Santoro, M. K. Nazeruddin and V. Barone, *J. Phys. Chem. B*, 2008, **112**, 13181–13183.
28 Y. Niu, Q. Peng, C. Deng, X. Gao and Z. Shuai, *J. Phys. Chem. A*, 2010, **114**, 7817.
29 K. Li, G. S. Ming Tong, Q. Wan, G. Cheng, W. Y. Tong, W. H. Ang, W. L. Kwong and C. M. Che, *Chem. Sci.*, 2016, **7**, 1653–1673.
30 F. De Angelis, F. Santoro, M. K. Nazeruddin and V. Barone, *J. Phys. Chem. B*, 2008, **112**, 13181–13183.
31 S. H. Lin, *J. Chem. Phys.*, 1970, **53**, 3766–3767.
32 S. H. Lin, C. H. Chang, K. K. Liang, R. Chang, Y. J. Shiu, J. M. Zhang, T. S. Yang, M. Hayashi and F. C. Hsu, *Adv. Chem. Phys.*, 2002, **121**, 1–88.
33 M. R. Son, Y. J. Cho, H. J. Son, D. W. Cho and S. O. Kang, *Phys. Chem. Chem. Phys.*, 2017, **19**, 32670–32677.
34 L. Shih-Chun, R. E. Harding, C. P. Shipley, S. G. Stevenson, P. L. Burn and I. D. W. Samuel, *J. Am. Chem. Soc.*, 2009, **131**, 16681–16688.
35 X. Zhang, D. Jacquemin, Q. Peng, Z. Shuai and D. Escudero, *J. Phys. Chem. C*, 2018, **122**, 6340–6347.
36 Q. Peng, Y. Yi, Z. Shuai and J. Shao, *J. Am. Chem. Soc.*, 2007, **129**, 9333–9339.
37 Y. Luo, Y. Xu, W. Zhang, W. Li, M. Li, R. He and W. Shen, *J. Phys. Chem. C*, 2016, **120**, 3462–3471.
38 D. Escudero, *Chem. Sci.*, 2016, **7**, 1262–1267.
39 D. Jacquemin and D. Escudero, *Chem. Sci.*, 2017, **8**, 7844–7850.
40 G. S. Tong, P. K. Chow, W. P. To, W. M. Kwok and C. M. Che, *Chem. – Eur. J.*, 2014, **20**, 6433–6443.
41 J. Z. Fan, L. L. Lin and C. K. Wang, *J. Mater. Chem. C*, 2017, **5**, 8390–8399.
42 G. Li, A. Wolfe, J. Brooks, Z. Q. Zhu and J. Li, *Inorg. Chem.*, 2017, **56**, 8244.

